High-fidelity patterning of AlN and ScAlN thin films with wet chemicaletching

Airola, Konsta

2022-05

Airola , K , Mertin , S , Likonen , J , Hartikainen , E , Mizohata , K , Dekker , J , Sebastian , A T & Pensala , T 2022 , ' High-fidelity patterning of AlN and ScAlN thin films with wet chemicaletching ' , Materialia , vol. 22 , 101403 . https://doi.org/10.1016/j.mtla.2022.101403

http://hdl.handle.net/10138/346085
https://doi.org/10.1016/j.mtla.2022.101403

Materialia 22 (2022) 101403

Contents lists available at ScienceDirect

Materialia

journal homepage: www.elsevier.com/locate/mtla

High-fidelity patterning of AlN and ScAlN thin films with wet chemical etching

Konsta Airola[a,*], Stefan Mertin[a], Jari Likonen[a], Enni Hartikainen[a], Kenichiro Mizohata[b], James Dekker[a], Abhilash Thanniyil Sebastian[a], Tuomas Pensala[a,‡]

[a] VTT Technical Research Centre of Finland Ltd, Espoo 02150, Finland.
[b] Department of Physics, University of Helsinki, P.O. Box 43, Helsinki FI-00014, Finland

ARTICLE INFO

Keywords:
Sputtering
Patterning
Piezoelectricity
Thin films
Scandium Aluminium Nitride

ABSTRACT

We report on the anisotropic wet etching of sputtered AlN and $Sc_{0.2}Al_{0.8}N$ thin films. With tetramethyl ammonium hydroxide at 80 °C, the etch rates along the *c*-axis were 330 and 30 nm/s for AlN and $Sc_{0.2}Al_{0.8}N$, respectively. Although the etching was anisotropic, significant lateral etching below the mask occurred, perpendicular to the *c*-axis. With a 1 µm $Sc_{0.2}Al_{0.8}N$ film, it could be up to 1800 nm. We studied the lateral etching with molybdenum, SiO_2, SiN_x and TiO_2 masks, and found the leading cause for the lateral etching to be modification of the AlN or $Sc_{0.2}Al_{0.8}N$ surface caused by ion bombardment and surface oxidation by ambient air. The lateral etching was reduced by optimizing the mask deposition and with thermal annealing. With $Sc_{0.2}Al_{0.8}N$, the lateral etching was reduced down to 35–220 nm depending on the mask, while with AlN, it was reduced to negligible. These results can be used for developing optimised mask deposition processes for better etch characteristics and for microfabrication of AlN and $Sc_xAl_{1-x}N$ thin-film structures.

1. Introduction

Aluminium nitride (AlN) is a piezoelectric material with the hexagonal wurtzite structure. It is widely applied in piezoelectric microelectromechanical systems (piezo-MEMS) due to its favourable properties and ease of process integration, including good etching characteristics with both wet and dry etching techniques [1–3]. The main drawback of AlN is its low piezoelectric coefficients, which limits its applications in devices where large piezoelectric response is beneficial.

To enhance the piezoelectric properties of AlN, some of the Al can be replaced with other metals [4,5]. Especially scandium aluminium nitride ($Sc_xAl_{1-x}N$) has gained considerable attention after its discovery in 2009 [6]. Replacing 37–43% of Al with Sc increases the longitudinal piezoelectric response from 8.4 pC/N up to 27.6 pC/N [6–8]. $Sc_xAl_{1-x}N$ maintains many of the excellent properties of AlN, including high sound velocity and thermal stability [9,10]. However, the deposition of high-quality $Sc_xAl_{1-x}N$ becomes more challenging with increasing *x*. Also, the material becomes more resistant to etching, especially with reactive ion etching (RIE).

Patterning of AlN has been studied for decades, and it can be done with both dry and wet etching. AlN is dry etched with plasmas consisting of Cl_2, BCl_3 and Ar, and etch rates can be up to 400 nm/min [11–15]. Typical sidewall angles are between 70 and 80 °. Wet etching can be done with both acidic and alkaline solutions, where AlN dissolves with the following reactions:

$$AlN + 4H^+ \rightarrow Al^{3+} + NH_4^+$$

$$AlN + OH^- + 3H_2O \rightarrow Al(OH)_4^- + NH_3$$

Common chemicals for etching AlN include KOH, tetramethyl ammonium hydroxide (TMAH) and H_3PO_4.

Wet etching of AlN is anisotropic. The etch rate of *c*-axis oriented AlN strongly depends on its polarity; etching the N-polar surface is up to 1000 times faster than etching the Al-polar surface [16]. Sputtering typically yields N-polar films which are well suited for patterning with wet etching [17–19]. In addition, the pyramidal planes of AlN are etched slower compared to the (000-1) plane. This results in the formation of cones with both polycrystalline and single crystal material during wet etching [16,20–22]. Examples include hexagonal cones defined by {10-1-1} planes in case of single crystal AlN and round cones defined by {10-1-2} planes with polycrystalline films [16,21].

Due to the anisotropic wet etching characteristics of AlN, it can be patterned with little deviation from the dimensions of the etch mask. The mask prevents the dissolution of the (000-1) plane, while the more stable pyramidal planes form the sidewalls [23]. However, a good interface between AlN and the mask material is required to prevent mask

* Corresponding author.
E-mail address: konsta.airola@vtt.fi (K. Airola).
‡ tuomas.pensala@vtt.fi

https://doi.org/10.1016/j.mtla.2022.101403
Received 28 December 2021; Accepted 20 March 2022
Available online 21 March 2022

undercutting. Lateral etching below the mask has often been reported, but to our knowledge, there is still a lack of detailed studies on minimising it [24–26].

Reported etch rates for N-polar AlN vary significantly between studies for several reasons. The etch rate depends significantly on the quality and microstructure of the material [24]. The etch rate of sputtered polycrystalline AlN can be orders of magnitude larger compared to single-crystal AlN [25]. For sputtered AlN films, the deposition conditions can affect the etch rate by at least a factor of four [20,26]. Substrate material and quality can also affect the etch rate [20,25]. Finally, due to the formation of cones with AlN, determining the etch rate is not straightforward, and often the exact measurement procedure has not been reported.

Despite the variation, reported wet etching rates for AlN are fast, especially with alkaline solutions. With H_3PO_4, the etch rates have been significantly slower. For sputtered AlN, etch rates up to 8000 nm/min have been reported with 25% TMAH at 82 °C [21]. With a solution of 80% H_3PO_4, 16% H_2O and 4% HNO_3, the etch rate was only 90 nm/min at 90 °C. In another study, with 15% KOH at room temperature, etch rates varied from 2.5 to 10 nm/s depending on the deposition conditions of the film [26]. The etch rates with 85% H_3PO_4 at 80 °C were 7-30 nm/min.

Although the etch rate can vary depending on the microstructure of the AlN, similar variation has not been observed with the activation energy. No significant dependence on the film quality, crystalline structure or deposition technique has been found [25,26]. The activation energy has been 57-67 kJ/mol with KOH, and 68.5–77 kJ/mol with H_3PO_4 [25 28].

$Sc_xAl_{1-x}N$ can also be patterned by both wet and dry etching. However, dry etching of $Sc_xAl_{1-x}N$ is challenging due to the low volatility of $ScCl_3$ [29]. The dry etch rate decreases rapidly with increasing x. With similar Cl-based etching recipes as used for AlN, addition of 20% Sc can reduce the etch rate by 80% [7,30]. Increasing the etch rate back to reasonable levels requires increased etching power and ion bombardment [30,31]. The low etch rate and high power requirements leads to poor selectivity to many mask materials, and over etching into the bottom layer may become a significant issue.

The poor dry etch characteristics makes wet etching of $Sc_xAl_{1-x}N$ an attractive alternative, but it has received little focus so far. Drawing conclusions about the wet etching is not possible from previous publications due to the vastly varying experimental conditions, but some earlier results are presented here for comparison. With MIF-319 developer containing 2.2% TMAH, the etch rate of $Sc_{0.15}Al_{0.85}N$ was reported as 50 nm/min at 60-70 °C, which was four times lower than the etch rate for AlN [30]. In another study, etching of a 500 nm $Sc_{0.36}Al_{0.64}N$ film took only 15 s with 25% KOH at 80 °C [32]. With 85% H_3PO_4 at 80 °C, the same material was not fully etched in 15 min and a large number of cones remained, which is consistent with the measured etch rate of 38.5 nm/min for $Sc_{0.35}Al_{0.65}N$ under similar conditions [33]. With 25% KOH, the removal time of 1 μm $Sc_{0.2}Al_{0.8}N$ has been reported at 7 min at 40 °C, or 25 min at room temperature [34]. To further understand the etching of $Sc_xAl_{1-x}N$, we aim to analyse and compare the wet etching of AlN and $Sc_{0.2}Al_{0.8}N$ in detail with a goal of minimizing the mask undercut and finding other relevant factors for developing wet etching processes for the materials.

A difference with wet etching $Sc_xAl_{1-x}N$ compared to pure AlN is that unlike Al, Sc is poorly soluble in alkaline solutions [35–37]. It does not tend to dissolve as $Sc(OH)_4^-$ even in strongly alkaline conditions. With our etching process, this resulted in the deposition of ScO_xH_y residues on the wafer surface requiring an added cleaning step in dilute acid as described later.

Finally, the etching of $Sc_xAl_{1-x}N$ is also made more difficult by the formation of abnormally oriented grains (AOGs) during deposition [38,39]. These are grains which have the correct wurtzite structure but are misoriented in relation to the desired c-axis growth [39]. AOGs are more likely to form with increasing x and they degrade the piezoelectric properties of the film and consequently the device performance [40–42]. In this work, we also show that the AOGs are more resistant to wet etching, which increases the etch time required to pattern the material, thus causing increased mask undercut.

2. Experimental

AlN and $Sc_{0.2}Al_{0.8}N$ thin films were deposited on 150 mm p-type (100) Si wafers with an Evatec Clusterline 200 II (CLN 200) cluster sputtering system with reactive magnetron sputtering. The 304 mm targets (Al and $Sc_{0.2}Al_{0.8}$) were driven with 7.5 kW pulsed direct current (pDC) power. Deposition temperature was 300 °C and the ratio of sputtering gas flows was set to 1:3 Ar:N_2. For stress control, a radio frequency (RF) bias power was put on the sputtering chuck (18 W for AlN and 12 W for $Sc_{0.2}Al_{0.8}N$ films). X-ray diffraction (XRD) rocking curve measurements were performed on an Panalytical X'pert Pro diffractometer using Cu K_α radiation, and the measurement was done at the wafer centre. Film thicknesses were measured with a Filmtek 2000 reflectometer.

Mo was deposited with five different processes, designated here as Mo-1-5 (Table 1). Mo-1-4 were deposited with the CLN 200. In the Mo-1 and -2 processes, the AlN or $Sc_{0.2}Al_{0.8}N$ films were exposed to air for at least a week before the Mo deposition. In the Mo-1 process, the film surface was cleaned using a 30 s inductively coupled plasma (ICP) soft etch process included in the tool. The etch gas was Ar and the ICP RF power was set to moderate 100 W to minimise sputter etch damage. In the Mo-2 process, the ICP plasma cleaning was omitted. In the Mo-3 and -4 processes, the $Sc_{0.2}Al_{0.8}N$ was not exposed to air after its deposition, but the Mo mask was deposited on it without vacuum break. In the Mo-3 process, the ICP plasma cleaning was included before the Mo deposition, while it was omitted in the Mo-4 process. Mo was deposited form a 100 mm target with 1 kW power and Ar as the sputtering gas. Deposition temperature was 200 or 300 °C, which did not have any effect on the etching.

Mo-5 was deposited with a Von Ardenne CS 730 S cluster sputtering system at room temperature. The 200 mm Mo target was driven by DC power at 1 kW. A suitable Ar flow was chosen for low film stress. Before the Mo deposition, the $Sc_{0.2}Al_{0.8}N$ surface was cleaned by an inverse sputter etch process using an Ar RF plasma ion gun (30 s, 200 W RF power). With all Mo processes, the Mo thickness was about 200 nm.

SiO_2 and SiN_x were deposited with an Oxford Instruments Plasmalab 100 plasma-enhanced chemical vapor deposition (PECVD) system. The precursors were SiH_4 and N_2O or NH_3, respectively. The deposition temperature was 300 °C. SiO_2 was deposited on $Sc_{0.2}Al_{0.8}N$ also using tetraethyl orthosilicate (TEOS) and O_2 as precursors with a deposition temperature of 350 °C. This is referred to as TEOS SiO_2. The thicknesses of these films were 150–200 nm.

TiO_2 was deposited with a Picosun R-150B atomic layer deposition (ALD) reactor. The precursors were $TiCl_4$ and H_2O, and the deposition temperature was 200 °C. 1000 deposition cycles were used, which yielded a 40 nm film.

After deposition, some of the masked AlN and $Sc_{0.2}Al_{0.8}N$ films were annealed with an ATV PEO-603 annealing furnace. Annealing was done in an N_2 atmosphere at atmospheric pressure and at temperatures of 550, 700 and 900 °C. The annealing cycle consisted of purging the furnace of air, heating at about 15 °C/min, holding at temperature for 1

Table 1
Summary of the Mo-deposition processes.

	Mo sputtering system	AlN/$Sc_{0.2}Al_{0.8}N$ air exposure	*In situ etch*
Mo-1	CLN 200	Yes	ICP
Mo-2	CLN 200	Yes	No
Mo-3	CLN 200	No	ICP
Mo-4	CLN 200	No	No
Mo-5	CS 730 S	Yes	Ion gun

hour, and cooling at about 15 °C/min. Stress changes were monitored by measuring the wafer curvature optically before and after annealing.

The wafers were patterned with standard photolithography techniques. The pattern was etched into the mask material with RIE. Mo and TiO_2 films were etched with a Surface Technology Systems Advanced Oxide Etcher. For Mo, etching gases were SF_6, O_2 and Ar, and for TiO_2, CF_4 was used. SiO_2 and SiN_x were etched with an Oxford Instruments Plasmalab 80plus RIE system, where CHF_3 and O_2 were used as the etching gases. After patterning of the mask, the photoresist was stripped with an Oxford Instruments PRS 901 plasma stripper using O_2 plasma.

For etching of the AlN or $Sc_{0.2}Al_{0.8}N$, the wafers were typically cleaved into 8 pieces. Etching of samples was done with 25 weight-% TMAH (2.8 mol/l) (danger: highly toxic) at temperatures of approximately 80, 60, 40 and 21 °C with an error of ±2 °C. 80 °C was used as the temperature for most experiments, and it is mentioned separately if a different temperature was used. No active stirring was applied to the solution during etching. The samples were rinsed with de-ionized water and dried by blowing with N_2. Also 85% H_3PO_4 and 4.5 mol/l H_2SO_4 at 80 °C were used for etching with the same procedure.

The etch rate of $Sc_{0.2}Al_{0.8}N$ was determined by measuring the thickness before and after partially etching the film with reflectometry. For AlN, this was impossible due to the extreme roughness of the film after partial etching. Instead, the etch rate was determined by visually observing the AlN film during etching. The etching was captured on video for accurately determining the etching time. The etching end point was defined as the moment when there was no visible thin-film interference or additional light absorption by the AlN. The full film removal time was determined by inspecting the etched films with a microscope for any remaining cones. The lateral etching and sidewall angle were determined by inspecting the samples with a scanning electron microscope (SEM) Zeiss Supra 35. The samples were cleaved and imaged cross-sectionally. The errors of the etch rates were estimated to be ±20% at maximum.

Time-of-flight elastic recoil detection analysis (TOF-ERDA) measurements were carried out with the 5 MV tandem accelerator at the University of Helsinki using a 35 MeV $^{79}Br^{+7}$ beam. The detection angle was 40 ° and sample tilt angle was 78 °. Secondary ion mass spectrometry (SIMS) measurements were done with a VG IX70S SIMS instrument using a 11 keV Cs-ion beam. The analysed elements were H, C, O, F, Al, Si, Sc and Mo. The SIMS results were compared by normalizing them using the Al-signal of each sample. The error of the SIMS measurements was estimated to be ±20% at maximum. An Oxford Instruments energy-dispersive X-ray spectrometer (EDX) connected to a Zeiss LEO 1560 SEM was used to measure the composition of residues which remained after etching.

3. Results

The AlN and $Sc_{0.2}Al_{0.8}N$ films deposited on (100) Si exhibited a columnar well-oriented *c*-axis structure. FWHMs of the (0002) reflection rocking curve measurements were at best 1.18 ° for AlN and 1.34 ° for $Sc_{0.2}Al_{0.8}N$. All $Sc_{0.2}Al_{0.8}N$ films exhibited some AOGs (Fig. 1a). The thicknesses of AlN and $Sc_{0.2}Al_{0.8}N$ films were both measured as 1020±25 nm.

We also measured the piezoelectric properties of the films, and they corresponded closely with the values published earlier. Details and results of those experiments will be published separately. Nevertheless, we note that the quality of $Sc_xAl_{1-x}N$ films deposited with a corresponding sputtering tool has been demonstrated to be excellent [43].

Before etching, some films were thermally annealed. This caused significant compressive stress in $Sc_{0.2}Al_{0.8}N$ films, while the stress of AlN films did not change more than ±50 MPa. Annealing $Sc_{0.2}Al_{0.8}N$ at 550 °C changed the stress by about –80 MPa, annealing at 700 °C changed the stress by –350 to –500 MPa, and annealing at 900 °C changed it by –800 MPa.

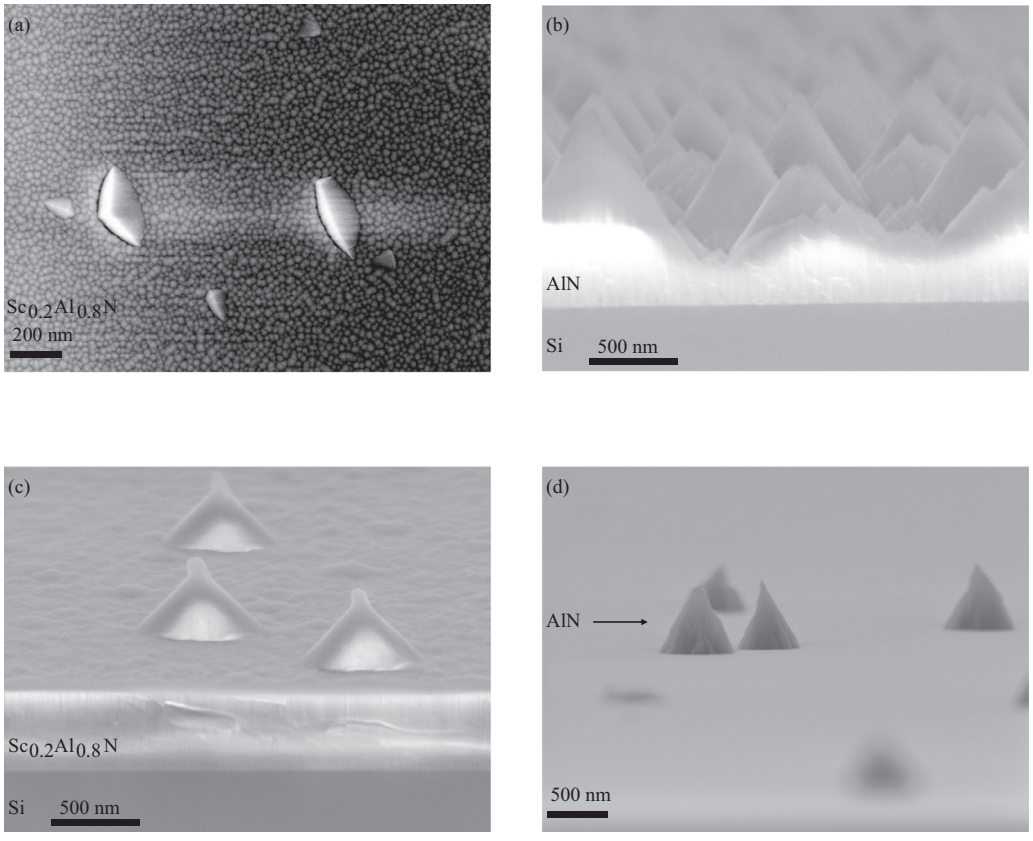

Fig. 1. (a) SEM top view of $Sc_{0.2}Al_{0.8}N$ film with AOGs, tilted cross-sectional images of (b) a partially etched AlN film, (c) a partially etched $Sc_{0.2}Al_{0.8}N$ film, (d) a mostly etched AlN film with 600 nm tall cones remaining.

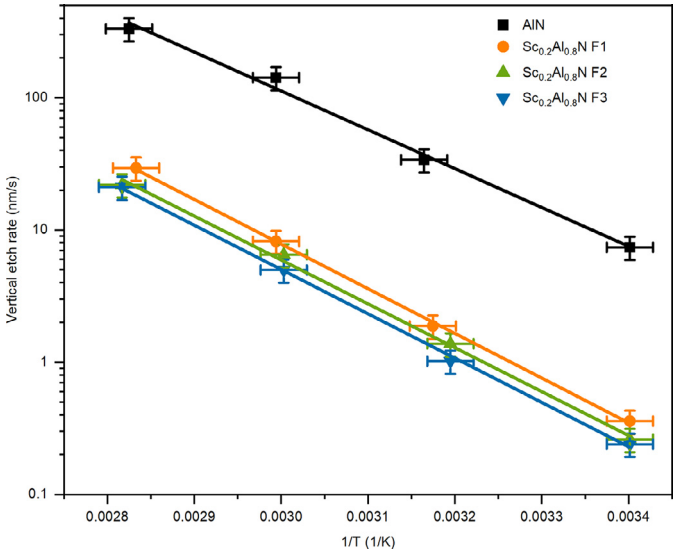

Fig. 2. Arrhenius plot of the vertical etch rates of AlN and three $Sc_{0.2}Al_{0.8}N$ films at temperatures of about 80, 60, 40 and 21°C with TMAH. The lines are fitted to the data points.

3.1. Etching mechanisms of AlN and $Sc_{0.2}Al_{0.8}N$

AlN and $Sc_{0.2}Al_{0.8}N$ films had vastly different etching mechanisms when etched with 25% TMAH. AlN formed a structure consisting of sharp cones with approximately 58 ° sidewall angle, which likely corresponds to the {10-1-1} planes (Fig. 1b). Due to this rapid coarsening of the film structure, the film thickness of partially etched AlN films could not be measured, and instead the etch rate was determined by visually observing the disappearance of the thin film during etching. The $Sc_{0.2}Al_{0.8}N$ films also formed cones during etching, but for a different reason compared to AlN. In the $Sc_{0.2}Al_{0.8}N$, cones were formed around AOGs, which were etched slower as compared to the rest of the film due to their misorientation (Fig. 1c). The sidewall angle of these cones was approximately 45°. Except for the AOGs, the *c*-axis oriented $Sc_{0.2}Al_{0.8}N$ was etched evenly with only minor coarsening.

Due to the formation of the cones with both films during etching, the etching of the films is described with three values: vertical etch rate, full film removal time and lateral etch rate. For AlN, the vertical etch rate is the inverse of the time required for the film to visually disappear. For $Sc_{0.2}Al_{0.8}N$, the vertical etch rate is based on the measured film thickness after partial etching. The full film removal time describes the time required to completely remove all cones. This was determined by inspecting the wafer surface with a microscope, where any remaining cones were easily visible as black spots (Fig. S1). The full film removal times were approximately 10–15 and 8 times longer than indicated by the vertical etch rate for AlN and $Sc_{0.2}Al_{0.8}N$, respectively. With both films, the etch rates of cones followed a distribution. Most cones were removed rapidly, while individual cones remained and required further etching to be fully removed (Fig. 1d). The lateral etch rate indicates how rapidly the material was etched sideways from bellow the mask.

Although the AlN and $Sc_{0.2}Al_{0.8}N$ films were deposited on Si, and TMAH is known to etch Si, no Si etching occurred except with overly long etching times.

3.2. Vertical etching of AlN and $Sc_{0.2}Al_{0.8}N$ with TMAH

At 80 °C, the vertical etching of AlN was extremely rapid (Fig. 2). The 1 μm thick film was etched in only about 3 s, corresponding to an etch rate of 330 nm/s (supplementary video 1). Pre-heating the sample to 80 °C before etching did not increase the etch rate observably. The etch rate of $Sc_{0.2}Al_{0.8}N$ was 10–15 times slower at 21–30 nm/s with some variation between different samples (Fig. 2). At 21 °C, the vertical etch rate of AlN was lowered to 7.4 nm/s, and for $Sc_{0.2}Al_{0.8}N$ it was 0.24–0.36 nm/s. The etching of $Sc_{0.2}Al_{0.8}N$ was very linear with increasing etching time (Fig. S2). The activation energy for the vertical etching of AlN was 56±8 kJ/mol, which is in agreement with the values published earlier [25 27]. For $Sc_{0.2}Al_{0.8}N$, it was 65±3 kJ/mol.

At 80 °C, the time required to remove the film fully with no cones remaining was 30 s for AlN and 5 min for $Sc_{0.2}Al_{0.8}N$. At 21 °C, the times were increased to 30 min and 6 h, respectively. Thermal annealing did not change the vertical etch rate. However, for $Sc_{0.2}Al_{0.8}N$, annealing at 700 °C increased the full film removal time at low etching temperatures. At 80 °C, the annealed films were still fully etched in 5 min, but at 21 °C the time was increased to approximately 12 h.

Table 2
Lateral etch rate (nm/s) of AlN with different mask materials with and without annealing with 3 min etching at 80 °C.

	Mo-1	SiO_2	SiN_x
As deposited	2.1–3.0	2.8	5.0
Annealed at 550 °C	1.0	0.39	
Annealed at 700 °C	0	0	0.22

3.3. Lateral etching of AlN with TMAH

Lateral etching of AlN was examined with three etch masks: Mo-1, SiO_2 and SiN_x. All masks were studied as deposited and after annealing at 700 °C. Mo-1 and SiO_2 were additionally studied after annealing at 550 °C. Table 2 summarizes the results with an etching time of 3 min.

With the Mo-1 and SiO_2 masks, the lateral etch rates were similar at 2.1–3.0 nm/s, corresponding to an undercut of 380-550 nm in 3 min (Fig. 3a). With the SiN_x mask, the lateral etch rate was higher at 5.0 nm/s. Annealing at 550 °C with the Mo-1 mask reduced the lateral etch rate to 1.0 nm/s, and with the SiO_2 mask, it was reduced to 0.39 nm/s. Annealing at 700 °C reduced the lateral etch rate even further. With the Mo-1 and SiO_2 masks, no lateral etching occurred in 3 min, while with the SiN_x mask, the undercut was 40 nm. 30 min etching with the annealed Mo-1 mask resulted in an undercut of 1.0 μm corresponding to a lateral etch rate of 0.55 nm/s.

The lateral etch rate of AlN depended significantly on the etching time. The lateral etching did not start immediately after immersing the sample into the TMAH, but it took tens of seconds to begin at 80 °C. At 21 °C it took tens of minutes correspondingly. With both Mo-1 and SiO_2 masks, the lateral etching was negligible at 30 s, and only 50 nm at 60 s. The origin of this time dependence is unclear. However, it enabled the patterning of AlN with minimal undercut even without annealing by choosing the minimum required etch time (Fig. 3b). This time dependence is not considered in the calculated lateral etch rates.

The effective lateral etching activation energy of AlN with the Mo-1 mask was 66±5 kJ/mol (Fig. 4), which was slightly higher compared to the activation energy for the vertical etching. This enabled reducing the undercut also by etching at lower temperatures. Lowering the etching temperature from 80 to 21 °C increased the selectivity between vertical and lateral etching by a factor of two. The term effective lateral etching activation energy is used as it varied based on the mask deposition process as shown later, and thus it is not an intrinsic material property. The sidewall angle of AlN after etching with TMAH was always 57–59° regardless of etching temperature, time, or annealing.

3.4. Lateral etching of $Sc_{0.2}Al_{0.8}N$ with TMAH

More lateral etching occurred with $Sc_{0.2}Al_{0.8}N$ compared to AlN. Therefore, the causes of the lateral etching and techniques for minimising it were investigated more in detail. The patterning of $Sc_{0.2}Al_{0.8}N$ was examined with all five differently deposited Mo masks. Four other masks were also tested: SiO_2, SiO_2 deposited from TEOS, SiN_x, and TiO_2.

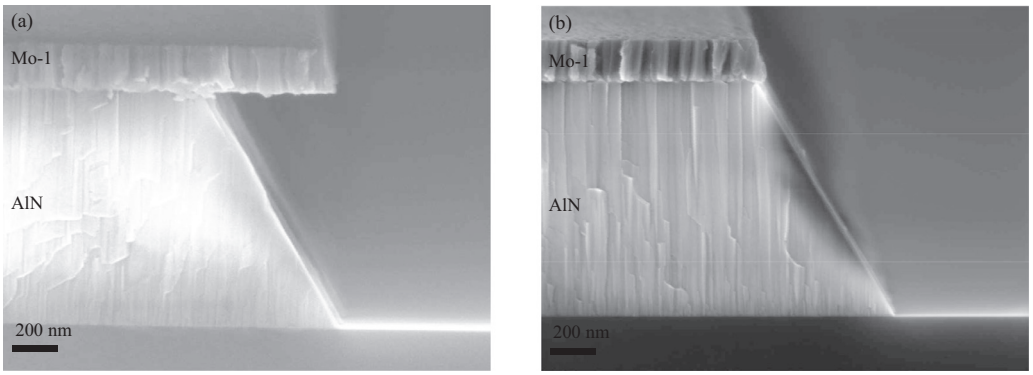

Fig. 3. AlN with Mo-1 mask after etching at 80°C for (a) 3 min or (b) 30 s.

Table 3
Lateral etch rates (nm/s) of $Sc_{0.2}Al_{0.8}N$ with different masks at 80 °C with 5 min etch time.

	Mo-1	Mo-2	Mo-3	Mo-4	Mo-5	SiO_2	TEOS SiO_2	SiN_x	TiO_2
As deposited	1.2–2.7	2.2	2.7	0.36	6.0	2.0–2.4	1.9	2.5	3.0
Annealed at 550 °C	0.73–1.2					0.60			
Annealed at 700 °C	0.53		0.60	0.45		0.60	0.73	0.57	0.73
Annealed at 900 °C	1.3					0.53			

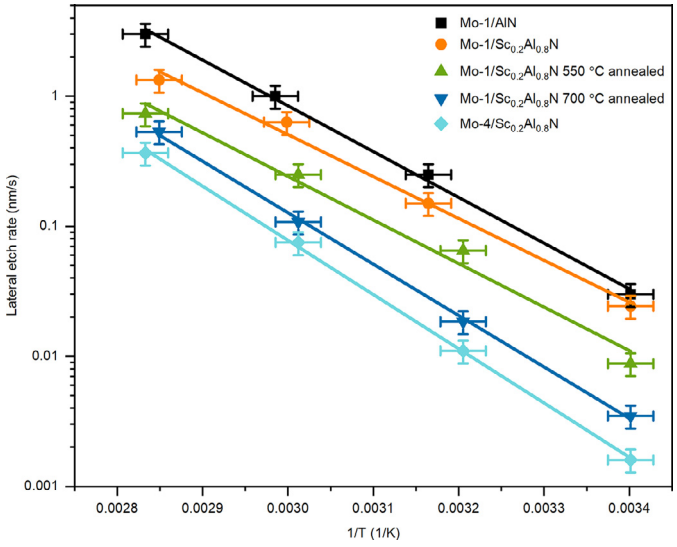

Fig. 4. Arrhenius plot for the lateral etching of AlN and $Sc_{0.2}Al_{0.8}N$ with Mo masks deposited with different processes. Etching was done at temperatures of about 80, 60, 40 and 21°C with TMAH. The lines are fitted to the data points.

Table 3 summarizes the lateral etch rates of $Sc_{0.2}Al_{0.8}N$ at 80 °C with the different masks.

When Mo was deposited on $Sc_{0.2}Al_{0.8}N$ with the Mo-1 process, which included exposing the $Sc_{0.2}Al_{0.8}N$ film to air and surface plasma cleaning before the Mo deposition, the lateral etch rate with TMAH varied from 1.1 nm/s to 2.7 nm/s. The reason for the variation was not discovered. The lateral etch rate corresponded to an undercut of 330–800 nm with a 5 min etch time. In the Mo-2 process, the film was exposed to air, but the plasma cleaning was not applied. This resulted in a lateral etch rate of 2.2 nm/s.

Mo was also deposited on $Sc_{0.2}Al_{0.8}N$ which had not been exposed to air. As the $Sc_{0.2}Al_{0.8}N$ and Mo films were sputtered with the same tool, they could also be deposited without breaking the vacuum in-between. This was done in the Mo-3 and Mo-4 processes. The Mo-3 process included the plasma clean, and the lateral etch rate was 2.7 nm/s. However, when the plasma cleaning was omitted in the Mo-4 process, the lateral etch rate was reduced to only 0.36 nm/s (Fig. 5a).

Finally, in the Mo-5 process, the Mo mask was deposited with a different sputtering tool (CS 730 S). Obviously, due to a sputtering tool change between the $Sc_{0.2}Al_{0.8}N$ and Mo, this deposition process included exposing the $Sc_{0.2}Al_{0.8}N$ film to air. A surface cleaning with a RF plasma sputter etch gun was also included before the Mo deposition. With this process, the lateral etch rate was 6.0 nm/s.

The effective lateral etching activation energy of $Sc_{0.2}Al_{0.8}N$ was 63±5 kJ/mol with the Mo-1 mask (Fig. 4). This was very similar to the activation energy of vertical etching, and the undercut could not be reduced by reducing the etching temperature. However, with the Mo-4 mask, the effective lateral etching activation energy was 78±5 kJ/mol (Fig. 4). By reducing the etching temperature, the selectivity between vertical and lateral etching was increased. A minimum undercut of 35 nm was achieved when $Sc_{0.2}Al_{0.8}N$ with the Mo-4 mask was etched at 21 °C for 6 h (Fig. 5b).

With the four other masks, the lateral etch rates were very close to each other, and they were also strikingly similar to the Mo-1, -2 and -3 masks. The lateral etch rates with SiO_2, TEOS SiO_2, SiN_x and TiO_2 masks were all between 1.9–3.0 nm/s (Fig. 5c). The effective lateral etching activation energy with a TEOS SiO_2 mask was 70±5 kJ/mol (Fig. S3), which was slightly higher compared to the effective activation energy with the Mo-1 mask.

Lateral etching of $Sc_{0.2}Al_{0.8}N$ with Mo-1 and SiO_2 masks was investigated with annealing at 550 °C. With the Mo-1 mask, the lateral etch rate was approximately halved. Similar variation occurred between different samples as with the as-deposited samples. With the SiO_2 mask, annealing at 550 °C reduced the lateral etch rate to only 0.60 nm/s. Annealing at 700 °C was studied with all masks except for Mo-2 and Mo-5. It reduced the lateral etch rate further to 0.53 nm/s with Mo-1 and to 0.60–0.73 nm/s with the other masks. With the Mo-4 mask, the lateral etch rate was slightly increased by the annealing (Fig. 5d). With the SiO_2 mask, annealing at 900 °C did not reduce the lateral etch rate significantly more compared to 700 °C. With the Mo-1 mask, annealing at 900 °C caused grain coarsening of the Mo layer and the lateral etch rate was increased to 1.3 nm/s (Fig. S4). Thermal annealing at 550 °C did not affect the effective lateral etching activation energy of $Sc_{0.2}Al_{0.8}N$

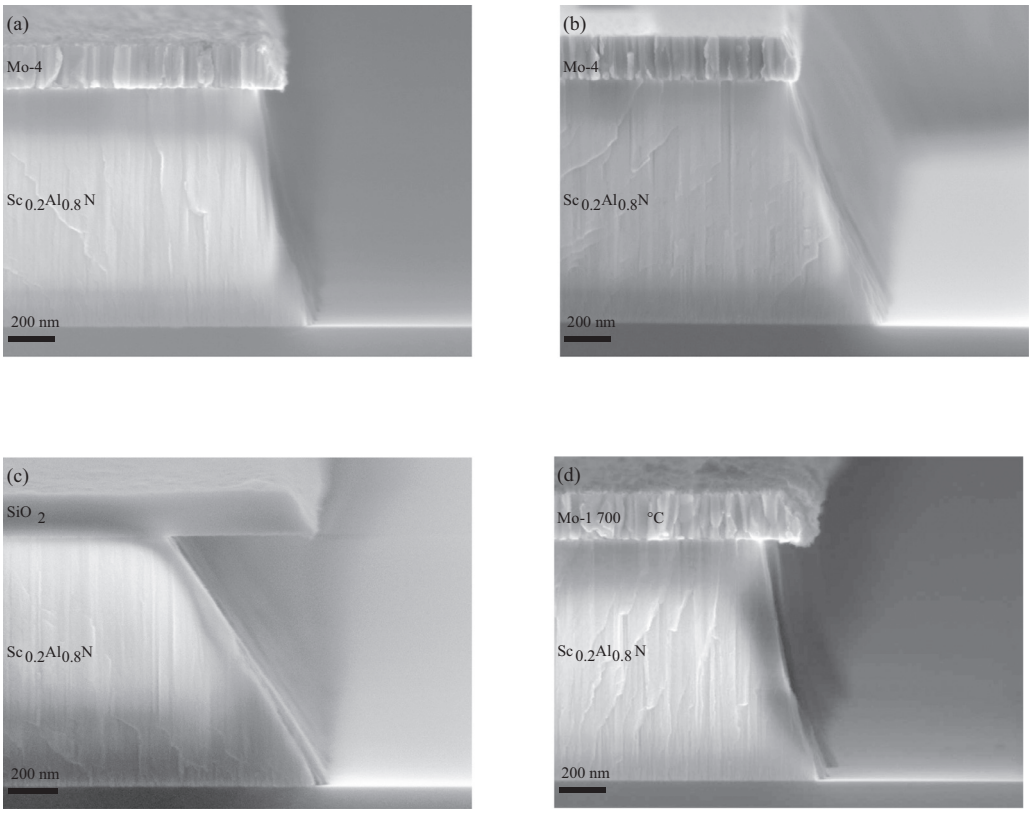

Fig. 5. $Sc_{0.2}Al_{0.8}N$ with (a) Mo-4 mask etched at 80°C for 5 min, (b) with Mo-4 mask etched at 21°C for 6 h, (c) SiO_2 mask etched at 80°C for 5 min, and (d) with Mo-1 mask annealed at 700°C and etched at 80°C for 5 min.

Table 4
Summary of acid etching of AlN and $Sc_{0.2}Al_{0.8}N$ films. (*Values were estimated by extrapolating from the experimental data).

	Mo-1/AlN	SiO_2/AlN	Mo-1/$Sc_{0.2}Al_{0.8}N$	SiO_2/ $Sc_{0.2}Al_{0.8}N$
H_3PO_4 vertical etch rate (nm/s)	8.3	8.3	2.8	2.8
Full film removal time (min)	10	10	30*	30*
Undercut with full film removal (nm)	50	700	10000*	15000*
H_2SO_4 vertical etch rate (nm/s)	0.55	0.55	0.28	
Full film removal time (min)	180*	180*	300*	
Undercut with full film removal (nm)	180*	540*	5500*	

but annealing at 700 °C increased it (Fig. 4, Fig. S3). With both Mo-1 and TEOS SiO_2 masks, the effective lateral etching activation energy was 77±5 kJ/mol after annealing at 700 °C.

The sidewall angle of $Sc_{0.2}Al_{0.8}N$ depended on the lateral etch rate of the film. With the masks exhibiting a lateral etch rate of 1.2–3.0 nm/s, the sidewall angle was 56–58° corresponding to the {10-1-1} planes (Fig. 5c). However, with the annealed masks and the Mo-4 mask with a lateral etch rate 0.73 nm/s or less, the sidewall angle was steeper at 70–80°. This indicates that the sidewall angle of $Sc_{0.2}Al_{0.8}N$ depended partially on the ratio of the vertical and lateral etch rates.

3.5. Etching of AlN and $Sc_{0.2}Al_{0.8}N$ with H_3PO_4 and H_2SO_4

Also 85% H_3PO_4 and 4.5 mol/l H_2SO_4 at 80 °C were tested for the patterning of AlN and $Sc_{0.2}Al_{0.8}N$. Both etchants had lower vertical etch rates and caused more lateral etching compared to TMAH (Table 4).

With H_3PO_4, the vertical etch rate of AlN was 8–9 nm/s, while it was about 3 nm/s for $Sc_{0.2}Al_{0.8}N$. The respective full film removal times were 10 and 30 min. AlN with the Mo-1 mask performed similar as with TMAH etching. With the minimum etch time of 10 min, the undercut was less than 50 nm. However, with the SiO_2 mask, the lateral etch rate was significantly higher at 1.2 nm/s. With $Sc_{0.2}Al_{0.8}N$, the performance was much worse. The lateral etch rates were 5.4 nm/s with Mo-1 and 8.3 nm/s with SiO_2 masks, respectively. Thermal annealing at 700 °C reduced the lateral etch rate to 1.6 nm/s for Mo-1 and 0.68 nm/s for SiO_2.

With H_2SO_4, the etch rates for both materials were significantly lower. The vertical etch rate for AlN was reduced to 0.55 nm/s, and for $Sc_{0.2}Al_{0.8}N$, it was 0.28 nm/s. These correspond to full film removal times of approximately 180 and 300 min. For AlN, the lateral etch rates were 0.017 nm/s with Mo-1 and 0.05 nm/s with SiO_2 masks. For $Sc_{0.2}Al_{0.8}N$, lateral etch rate was 0.28 nm/s with the Mo-1 mask.

With the acidic etchants, the sidewall angles were different from those observed with TMAH. The sidewall angle of AlN was 54–56° when etched with H_3PO_4 but only 38–42° with H_2SO_4 (Fig. 6a). The sidewall angles of $Sc_{0.2}Al_{0.8}N$ were 29-31° with H_3PO_4, and 25–27° with H_2SO_4 (Fig. 6b, c). However, the sidewall angle for $Sc_{0.2}Al_{0.8}N$ etched with H_3PO_4 was likely caused by the large lateral etch rate. When annealed $Sc_{0.2}Al_{0.8}N$ was etched with H_3PO_4, the sidewall angle was increased to 42–48°. This can also be observed in Fig. 6c, where the sidewall angle

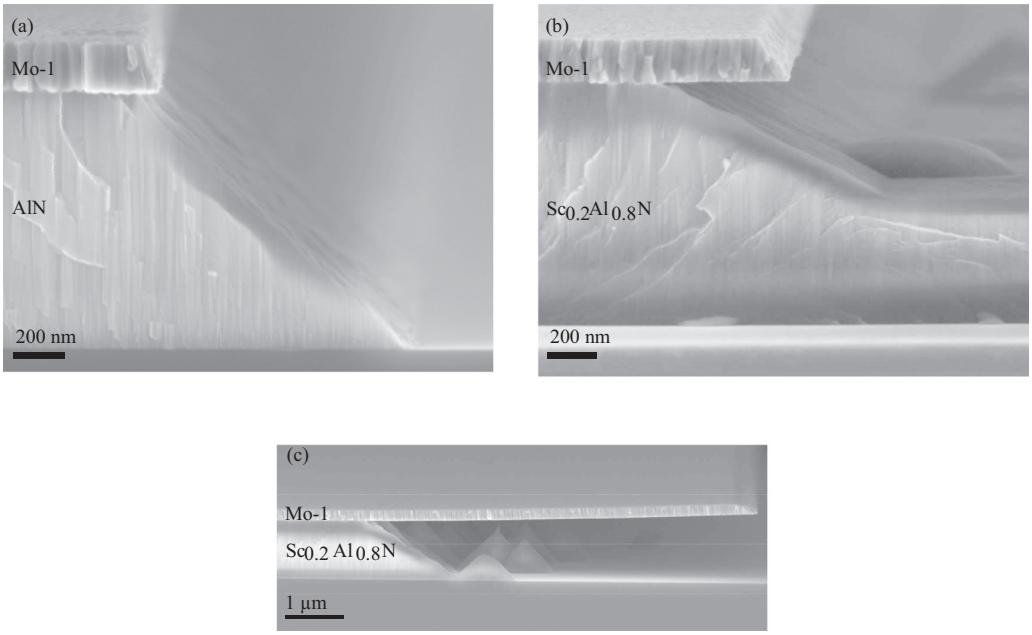

Fig. 6. (a) AlN etched with H_2SO_4 for 90 min, (b) $Sc_{0.2}Al_{0.8}N$ etched with H_2SO_4 for 30 min, (c) $Sc_{0.2}Al_{0.8}N$ etched with H_3PO_4 for 20 min.

of the cones is significantly larger compared to the masked $Sc_{0.2}Al_{0.8}N$. With H_2SO_4 however, the small sidewall angle of 25–27° was consistent between the masked material and the cones.

3.6. TOF-ERDA and SIMS measurements

The oxidation of $Sc_{0.2}Al_{0.8}N$ with the differently deposited Mo-masks was further investigated with TOF-ERDA and SIMS. A $Sc_{0.2}Al_{0.8}N$ reference sample and $Sc_{0.2}Al_{0.8}N$ with the Mo-2 mask were measured with TOF-ERDA, while SIMS was used to investigate $Sc_{0.2}Al_{0.8}N$ with the Mo-1 (2 samples), Mo-2, Mo-2 annealed at 550 ˚C, Mo-3 and Mo-4 masks and a $Sc_{0.2}Al_{0.8}N$ reference.

According to the TOF-ERDA measurements, the $Sc_{0.2}Al_{0.8}N$ reference film had an expected (Sc+Al)/N ratio close to 1 (0.97) and a Sc/(Sc+Al) concentration of 19.2±0.3%, which was slightly lower than the nominal 20% Sc of the target. The film had only 0.24% H and 0.37% O as impurities with the surface excluded (Table S1). The surface had much higher concentration of O, corresponding to an oxide layer of about 6–7 nm (Fig. S5) which is comparable to previous results [7]. The surface also had more H compared to the rest of the film. Measurement of the Mo-2/$Sc_{0.2}Al_{0.8}N$ sample showed similar oxide thickness and H-concentration on the $Sc_{0.2}Al_{0.8}N$ surface as compared to the reference (Fig. 7a). There were little impurities in the Mo-layer except for some surface oxide.

SIMS measurements showed high amounts of O on the $Sc_{0.2}Al_{0.8}N$ surface with the Mo-2 mask (Fig. 7b). However, even with the plasma cleaning in the Mo-1 process, approximately half to quarter of the native surface oxide layer of the $Sc_{0.2}Al_{0.8}N$ film remained depending on the sample. With the Mo-3 and Mo-4 masks, the $Sc_{0.2}Al_{0.8}N$ film had one tenth or less of the surface oxide compared to the Mo-2 mask. The similarity with Mo-3 and -4 masks demonstrated that the plasma cleaning before the Mo deposition did not cause any further formation of surface oxide.

During the SIMS measurements, with the Mo-1 and Mo-2 samples, the Sc- and Al-signals increased slowly to their maximum values at the Mo/$Sc_{0.2}Al_{0.8}N$ interface. However, with the Mo-3 and Mo-4 samples, the Sc- and Al-signals reached their maximums rapidly (Fig. 7b, Fig. S6a). This was likely due to reduced erosion rate of the $Sc_{0.2}Al_{0.8}N$ surface caused by the interface oxide on the Mo-1 and Mo-2 samples. The SIMS measurements showed a H-peak on the $Sc_{0.2}Al_{0.8}N$ surface only with the reference and Mo-2 samples (Fig. S6b). With the other samples, the H-concentration was close to the bulk of the film. However, with the Mo-1/$Sc_{0.2}Al_{0.8}N$ samples, this cannot be taken for granted due to the reduced erosion rate at the interface. Annealing the Mo-2/$Sc_{0.2}Al_{0.8}N$ sample at 550 ˚C reduced the H-concentration by about 75%. The SIMS measurements did not give any substantial signal from the Mo-layer, and the full SIMS-spectra are available in Fig. S7.

3.7. Scandium residues

The poor solubility of scandium in alkaline solutions led to the formation and deposition of ScO_xH_y-residues on the wafer surface when taken out of the TMAH solution and rinsed (Fig. 8a, b). The residue formed a uniform layer on a portion of the wafer, while minor depositions occurred across the entire surface. The uniform layer was up to 150 nm thick. The Sc and O components of the residue were identified with EDX (Fig S8). The deposition of the residues depended on the sample size. With full 150 mm wafers, a significant amount of residues typically remained on the wafer surface. With the 1/8 wafer pieces used for most experiments, the residues were rarely observed.

The deposition of the residues also depended strongly on the rinsing method. More residues were deposited when a quick dump rinse was used, which quickly emptied and filled the rinsing tank, compared to an overflow rinse, which used continuous water flow to rinse the samples. However, we did not find any technique for completely avoiding the residues including manual agitation during etching. Instead, the residues could be easily removed in minutes even with weakly acidic solutions such as 0.1% H_3PO_4 and 1% HF.

4. Discussion

High-fidelity patterning of AlN and $Sc_xAl_{1-x}N$ can be challenging regardless if it is done with dry or wet etching. The difficulty in dry etching is the low volatility of $ScCl_3$, which reduces the etch rate significantly compared to AlN. With wet etching, the main problem is lateral etching below the mask. However, if the lateral etching during wet etching is not a concern, or if can be reduced to acceptable levels, wet etching becomes a very attractive option. Our experiments demonstrate that reducing the undercut to less than 50 nm for a patterned 1 um film is possible with both AlN and $Sc_{0.2}Al_{0.8}N$.

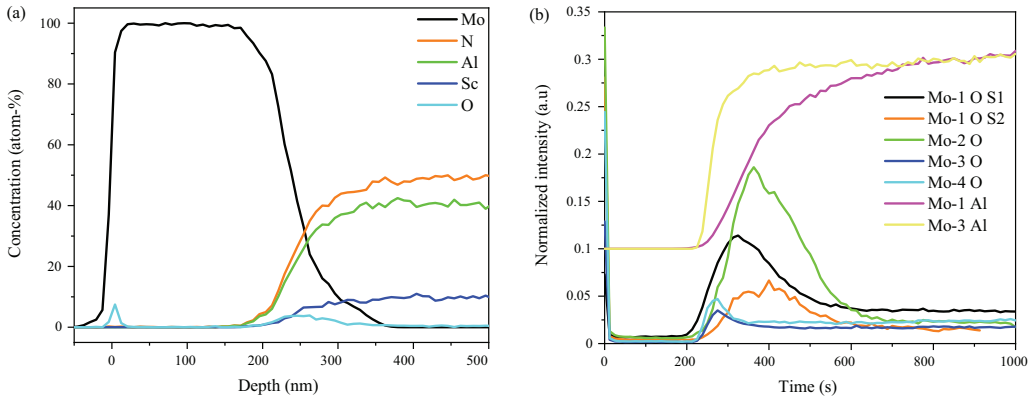

Fig. 7. (a) TOF-ERDA results of Mo-2/$Sc_{0.2}Al_{0.8}N$, (b) SIMS O-signal at the Mo/ $Sc_{0.2}Al_{0.8}N$ interface with the Mo-1 (2 samples), -2, -3 and -4 masks and the Al-signal with the Mo-1 and Mo-3 masks. The signals were normalized using the bulk Al-signal of the respective sample, and the Al-signals have been offset by 0.1.

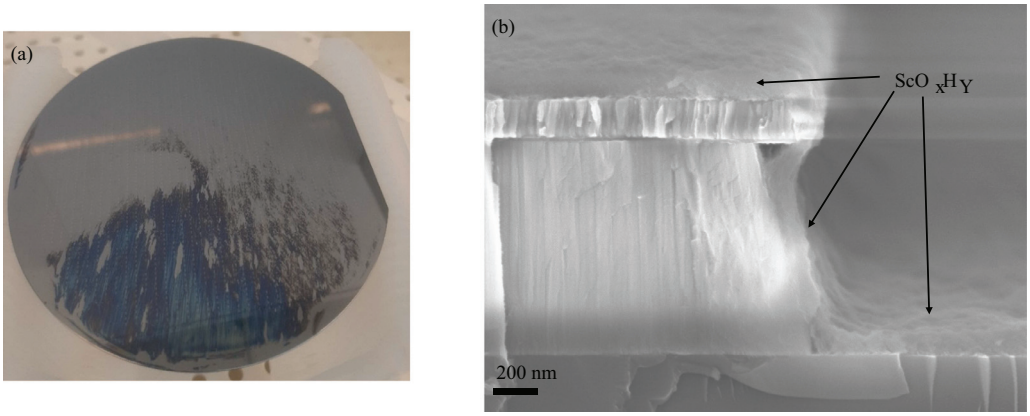

Fig. 8. ScO_xH_y-residue on a wafer surface after etching and using a quick-dump rinse, (b) cross-sectional image of etched $Sc_{0.2}Al_{0.8}N$ with a uniform 150 nm-thick ScO_xH_y layer.

The first requirement for a good AlN and $Sc_xAl_{1-x}N$ wet etching process is choosing a good etchant. TMAH performed well for both AlN and $Sc_{0.2}Al_{0.8}N$, and H_3PO_4 was a decent etchant for AlN but not for $Sc_{0.2}Al_{0.8}N$. H_2SO_4 performed poorly with both films. Based on these results, alkaline etchants are expected to perform better compared to acidic etchants. NaOH and KOH could perform also well for AlN and $Sc_xAl_{1-x}N$ etching if the alkali metal contamination can be tolerated. In addition, they are not toxic, which advocates their use over TMAH.

Second requirement for minimizing undercut during wet etching is optimization of the etching time. It should be as short as possible while still removing the film. If some cones remaining after etching could be accepted, it would enable reducing the etching time. The film thickness should also be as thin as possible, as it enables faster removal of the film and consequently less undercutting.

The choice of mask material had little effect on the lateral etch rate with both AlN and $Sc_{0.2}Al_{0.8}N$, especially when the films were exposed to air and no plasma cleaning was applied. This leaves surface oxidation of the AlN and $Sc_{0.2}Al_{0.8}N$ films as the most likely cause for the lateral etching with films exposed to air. Both AlN and $Sc_xAl_{1-x}N$ form a native oxide layer of a few nanometres when exposed to air, and the oxide thickness increases with x [7,39]. The TOF-ERDA measurements showed an oxide layer of approximately 7 nm on $Sc_{0.2}Al_{0.8}N$ exposed to air.

The lateral etch rates of $Sc_{0.2}Al_{0.8}N$ with the differently deposited Mo masks indicate that in addition to surface oxidation, surface damage caused by ion bombardment during plasma cleaning before mask deposition increased the lateral etch rate. Although the lateral etch rates between the Mo-1, -2 and -3 masks were similar, this was likely a coincidence and the main cause of the lateral etching was different between the masks. The role of the plasma cleaning in the Mo-1 and Mo-5 processes was to remove the surface oxide. However, the 30 s plasma cleaning was not sufficient at removing all oxide and no consistent reduction in the lateral etch rate occurred compared to the Mo-2 process or to the other mask materials. Also, with the Mo-3 process, which included the plasma cleaning, the lateral etch rate was increased significantly compared to the Mo-4 process. The SIMS measurements showed that the plasma cleaning did not introduce additional contaminants, which leaves damage by ion bombardment as the only evident cause of the increased lateral etch rate with the Mo-3 mask. With the Mo-5 process, which included a harsher surface cleaning, the lateral etch rate was significantly higher compared to any of the other Mo masks. Previously, ion bombardment has been shown to increase the etch rate of GaN under similar conditions as in this work [44]. Significant reductions in the lateral etch rate may be obtained if the cleaning is further optimized for removing the surface oxide with minimal surface damage.

Thermal annealing was an effective method for reducing the lateral etching by a factor of 3–5 for $Sc_{0.2}Al_{0.8}N$ which had been exposed to air or ion bombardment. The reduction with AlN was at least equal or even better. With the films which were exposed to air, the annealing increased the etch resistance of the surface oxide. Annealing is known to often reduce the etch rate of amorphous materials including Al_2O_3 [45,46]. The surface oxide hardened already with annealing at 550 °C. With the $Sc_{0.2}Al_{0.8}N$ and AlN films exposed to ion bombardment during the plasma clean, the annealing likely repaired some of the surface damage and 700 °C was required to minimize the effect of ion bombardment

on the lateral etching. In addition, annealing can also enhance the piezoelectric properties of $Sc_xAl_{1-x}N$, which further advocates for adding an annealing step to $Sc_xAl_{1-x}N$ processing [9,34,47–49].

A large disadvantage with annealing the $Sc_{0.2}Al_{0.8}N$ films was the compressive stress caused by it. The stress may be linked to changes in the lattice parameters of the film. In a previous study, the *c*-axis constant of sputtered $Sc_xAl_{1-x}N$ on sapphire was found to decrease with thermal annealing [9]. However, the *a*-axis constant or the stress did not change significantly. More studies on the effect of annealing on the $Sc_xAl_{1-x}N$ microstructure are needed to explain the stress changes we observed.

For $Sc_xAl_{1-x}N$, the film quality is extremely important. In addition to the reduced piezoelectric response, films with large number of AOGs are more difficult to etch. Increased number of AOGs leads to an increased number of cones formed during etching, which may increase the chance of device failure if all cones are not fully removed. On the other hand, if no AOGs are formed during deposition, according to our results there should not be any formation of cones enabling reduced etching times. However, in a previous study, partial etching of $Sc_xAl_{1-x}N$ films resulted in uneven etching and a high number of cones similar to AlN [32]. The cones were not associated with AOGs, which suggests there may be other mechanisms than AOGs which result in cone formation during etching of $Sc_xAl_{1-x}N$, but those were not observed here.

The sidewall angles with $Sc_{0.2}Al_{0.8}N$ varied much more compared to AlN and they were dependent on the lateral etch rate. Also, $Sc_{0.2}Al_{0.8}N$ film did not form cones during etching except for around AOGs. This suggests that the chemical stability of the {10-1-1} planes is reduced with the addition of Sc to AlN. This may enable further controlling the sidewall angle during wet etching by tuning the mask deposition and etching conditions.

While alkaline etchants appear to be generally superior over acidic etchants for $Sc_xAl_{1-x}N$, the possible appearance of insoluble residues must be accounted for. The rinsing should be done carefully by overflowing the rinsing bath. Still, cleaning the wafers afterwards with acid may be required to completely avoid the residues.

5. Conclusions

We studied the factors that affect the vertical and lateral etch rates of AlN and $Sc_{0.2}Al_{0.8}N$ during wet etching. TMAH, H_3PO_4 and H_2SO_4 were tested as etchants, with TMAH having the best performance, and the patterning process was optimized for it. For AlN, the etch rate was very high at 330 nm/s at 80 °C, but the film required significant over etching due to the formation of slow-etching conical features. However, choosing the minimum required etch time of 30 s enabled high-quality patterning with no lateral etching. The etch rate of $Sc_{0.2}Al_{0.8}N$ was lower at 20–30 nm/s, and the required time to etch the 1 μm film completely was 5 min. With this etching time, 600–900 nm of lateral etching occurred with most mask materials. The main causes for the lateral etching were surface oxidation and ion-bombardment induced surface damage during plasma cleaning before the mask deposition, with the choice of mask material having only little effect. The lateral etching of $Sc_{0.2}Al_{0.8}N$ was reduced to 35 nm by eliminating the surface oxidation and damage, or to 150–220 nm by reducing the effect of these defects with thermal annealing. These results can be applied for fabricating devices with AlN and $Sc_{0.2}Al_{0.8}N$ and as a baseline for developing patterning processes for other $Sc_xAl_{1-x}N$ compositions. The discovered causes behind the lateral etching can be used for developing mask deposition processes for better etching of AlN and $Sc_xAl_{1-x}N$.

Availability of data and material

The datasets generated during the current study are available from the corresponding author on reasonable request.

Author contributions

K.A. planned the study, partially prepared, patterned and analysed the samples, and wrote the initial manuscript, S.M. and E.H. deposited AlN, $Sc_{0.2}Al_{0.8}N$, and Mo films, J.L. did SIMS measurements, E.H. characterized AlN and $Sc_{0.2}Al_{0.8}N$ films, K.M. did TOF-ERDA measurements, J.D. supervised K.A., A.T.S. assisted with sample preparation, T.P. planned and supervised the project under which the work was performed. All authors commented on the manuscript

Declaration of Competing Interest

The authors have declared no conflicts of interest.

Acknowledgements

The authors would like to thank Marcelo Rizzo Piton for assistance with EDX measurements. The work was done in the BeyondSOI project funded by Business Finland and VTT.

Supplementary materials

Supplementary material associated with this article can be found, in the online version, at doi:10.1016/j.mtla.2022.101403.

References

[1] W.R. Ali, M. Prasad, Piezoelectric MEMS based acoustic sensors: A review, Sensors Actuators A Phys 301 (2020) 111756, doi:10.1016/j.sna.2019.111756.
[2] G. Pillai, S.S. Li, Piezoelectric MEMS resonators: a review, IEEE Sens. J. 21 (2021) 12589–12605, doi:10.1109/JSEN.2020.3039052.
[3] S. Tadigadapa, K. Mateti, Piezoelectric MEMS sensors: State-of-the-art and perspectives, Meas. Sci. Technol. 20 (2009) 092001, doi:10.1088/0957-0233/20/9/092001.
[4] S. Manna, K.R. Talley, P. Gorai, J. Mangum, A. Zakutayev, G.L. Brennecka, V. Stevanović, C.V. Ciobanu, Enhanced piezoelectric response of AlN via CrN alloying, Phys. Rev. Appl. 9 (2018) 1–10, doi:10.1103/PhysRevApplied.9.034026.
[5] K. Hirata, H. Yamada, M. Uehara, S.A. Anggraini, M. Akiyama, First-principles study of piezoelectric properties and bonding analysis in (Mg, X, Al)N solid solutions (X = Nb, Ti, Zr, Hf), ACS Omega 4 (2019) 15081–15086, doi:10.1021/acsomega.9b01912.
[6] M. Akiyama, T. Kamohara, K. Kano, A. Teshigahara, Y. Takeuchi, N. Kawahara, Enhancement of piezoelectric response in scandium aluminum nitride alloy thin films prepared by dual reactive cosputtering, Adv. Mater. 21 (2009) 593–596, doi:10.1002/adma.200802611.
[7] R. Petrich, H. Bartsch, K. Tonisch, K. Jaekel, S. Barth, H. Bartzsch, D. Glos, A. Delan, S. Krischok, S. Strehle, M. Hoffmann, J. Muller, Investigation of ScAlN for piezoelectric and ferroelectric applications, 2019 22nd Eur. Microelectron. Packag. Conf. Exhib. (2019), doi:10.23919/EMPC44848.2019.8951824.
[8] O. Zywitzki, T. Modes, S. Barth, H. Bartzsch, P. Frach, Effect of scandium content on structure and piezoelectric properties of AlScN films deposited by reactive pulse magnetron sputtering, Surf. Coatings Technol. 309 (2017) 417–422, doi:10.1016/j.surfcoat.2016.11.083.
[9] P.M. Mayrhofer, P.O.Å. Persson, A. Bittner, U. Schmid, Properties of $Sc_xAl_{1-x}N$ (x = 0.27) thin films on sapphire and silicon substrates upon high temperature loading, Microsyst. Technol. 22 (2016) 1679–1689, doi:10.1007/s00542-015-2798-7.
[10] F. Parsapour, V. Pashchenko, N. Kurz, C.S. Sandu, T. LaGrange, K. Yamashita, V. Lebedev, P. Muralt, Material parameter extraction for complex AlScN thin film using dual mode resonators in combination with advanced microstructural analysis and finite element modeling, Adv. Electron. Mater. 5 (2019) 1–9, doi:10.1002/aelm.201800776.
[11] H. Okumura, Fabrication of an AlN ridge structure using inductively coupled Cl_2/BCl_3 plasma and a TMAH solution, Jpn. J. Appl. Phys. 58 (2019) 3–7, doi:10.7567/1347-4065/aaf78b.
[12] H.S. Kim, D.H. Lee, J.W. Lee, T.I. Kim, G.Y. Yeom, Effects of plasma conditions on the etch properties of AlGaN, Vacuum 56 (2000) 45–49, doi:10.1016/S0042-207X(99)00156-6.
[13] V. Bliznetsov, B.H. Bin Johari, M.T. Chentir, W.H. Li, L.Y. Wong, S. Merugu, X.L. Zhang, N. Singh, Improving aluminum nitride plasma etch process for MEMS applications, J. Micromechanics Microeng. 23 (2013) 117001, doi:10.1088/0960-1317/23/11/117001.
[14] F.A. Khan, L. Zhou, V. Kumar, I. Adesida, R. Okojie, High rate etching of AlN using $BCl_3/Cl_2/Ar$ inductively coupled plasma, Mater. Sci. Eng. B Solid-State Mater. Adv. Technol. 95 (2002) 51–54, doi:10.1016/S0921-5107(02)00160-5.
[15] X. Liu, C. Sun, B. Xiong, L. Niu, Z. Hao, Y. Han, Y. Luo, Smooth etching of epitaxially grown AlN film by Cl_2/BCl_3/Ar-based inductively coupled plasma, Vacuum 116 (2015) 158–162, doi:10.1016/j.vacuum.2015.03.030.

[16] W. Guo, J. Xie, C. Akouala, S. Mita, A. Rice, J. Tweedie, I. Bryan, R. Collazo, Z. Sitar, Comparative study of etching high crystalline quality AlN and GaN, J. Cryst. Growth. 366 (2013) 20–25, doi:10.1016/j.jcrysgro.2012.12.141.

[17] P. Muralt, in: AlN Thin Film Processing and Basic Properties, in: Microsystems Nanosyst, Springer International publishing, 2017, pp. 3–37, doi:10.1007/978-3-319-28688-4_1. Cham.

[18] E. Milyutin, S. Harada, D. Martin, J.F. Carlin, N. Grandjean, V. Savu, O. Vaszquez-Mena, J. Brugger, P. Muralt, Sputtering of (001)AlN thin films: control of polarity by a seed layer, J. Vac. Sci. Technol. B. 28 (2010) L61–L63, doi:10.1116/1.3501117.

[19] E. Wistrela, M. Schneider, A. Bittner, U. Schmid, Impact of the substrate dependent polarity distribution in c-axis oriented AlN thin films on the etching behaviour and the piezoelectric properties, Microsyst. Technol. 22 (2016) 1691–1700, doi:10.1007/s00542-015-2799-6.

[20] S.M. Tanner, V.V. Felmetsger, Microstructure and chemical wet etching characteristics of AlN films deposited by ac reactive magnetron sputtering, J. Vac. Sci. Technol. A. 28 (2010) 69–76, doi:10.1116/1.3268620.

[21] S. Marauska, V. Hrkac, T. Dankwort, R. Jahns, H.J. Quenzer, R. Knöchel, L. Kienle, B. Wagner, Sputtered thin film piezoelectric aluminum nitride as a functional MEMS material, Microsyst. Technol. 18 (2012) 787–795, doi:10.1007/s00542-012-1493-1.

[22] D. Zhuang, J.H. Edgar, L. Liu, B. Liu, L. Walker, Wet chemical etching of AlN single crystals, MRS Internet J. Nitride Semicond. Res. 7 (2002) 1–6, doi:10.1557/s1092578300000302.

[23] S. Saravanan, E. Berenschot, G. Krijnen, M. Elwenspoek, A novel surface micromachining process to fabricate AlN unimorph suspensions and its application for RF resonators, Sensors Actuators A Phys 130–131 (2006) 340–345, doi:10.1016/j.sna.2005.09.029.

[24] I. Cimalla, C. Foerster, V. Cimalla, V. Lebedev, D. Cengher, O. Ambacher, Wet chemical etching of AlN in KOH solution, Phys. Status Solidi Curr. Top. Solid State Phys 3 (2006) 1767–1770, doi:10.1002/pssc.200565206.

[25] J.R. Mileham, S.J. Pearton, C.R. Abernathy, J.D. MacKenzie, R.J. Shul, S.P. Kilcoyne, Patterning of AlN, InN, and GaN in KOH-based solutions, J. Vac. Sci. Technol. A. 14 (1996) 836–839, doi:10.1116/1.580399.

[26] A. Ababneh, H. Kreher, U. Schmid, Etching behaviour of sputter-deposited aluminium nitride thin films in H_3PO_4 and KOH solutions, Microsyst. Technol. 14 (2008) 567–573, doi:10.1007/s00542-007-0450-x.

[27] W. Guo, R. Kirste, I. Bryan, Z. Bryan, L. Hussey, P. Reddy, J. Tweedie, R. Collazo, Z. Sitar, KOH based selective wet chemical etching of AlN, $Al_xGa_{1-x}N$, and GaN crystals: A way towards substrate removal in deep ultraviolet-light emitting diode, Appl. Phys. Lett. 106 (2015) 1–5, doi:10.1063/1.4913705.

[28] Y. ha Choi, K.H. Baik, R. Choi, J. Oh, J. Kim, Photo-enhanced acid chemical etching of high-quality aluminum nitride grown by metal-organic chemical vapor deposition, ECS J. Solid State Sci. Technol. 8 (2019) N42–N46, doi:10.1149/2.0051903jss.

[29] M.T. Hardy, B.P. Downey, D.J. Meyer, N. Nepal, D.F. Storm, D.S. Katzer, Epitaxial ScAlN etch-stop layers grown by molecular beam epitaxy for selective etching of AlN and GaN, in: Proceedings of the CS MANTECH 2017 - 2017 Int. Conf. Compd. Semicond. Manuf. Technol, 2017, pp. 475–479.

[30] Q. Wang, Y. Lu, S. Mishin, Y. Oshmyansky, D.A. Horsley, Design, fabrication, and characterization of scandium aluminum nitride-based piezoelectric micromachined ultrasonic transducers, J. Microelectromechanical Syst. 26 (2017) 1132–1139, doi:10.1109/JMEMS.2017.2712101.

[31] Y. Kusano, I. Ishii, T. Kamiya, A. Teshigahara, G.-L. Luo, D.A. Horsley, High-SPL air-coupled piezoelectric micromachined ultrasonic transducers based on 36% ScAlN thin-film, IEEE Trans. Ultrason. Ferroelectr. Freq. Control. 66 (2019) 1488–1496, doi:10.1109/TUFFC.2019.2921983.

[32] S. Fichtner, N. Wolff, F. Lofink, L. Kienle, B. Wagner, AlScN: A III-V semiconductor based ferroelectric, J. Appl. Phys. 125 (2019) 114103, doi:10.1063/1.5084945.

[33] T.-N. Kreutzer, S. Fichtner, B. Wagner, F. Lofink, A double-layer MEMS actuator based on ferroelectric polarization inversion in AlScN, in: 2021 IEEE Int. Symp. Appl. Ferroelectr, IEEE, 2021, pp. 1–3, doi:10.1109/ISAF51943.2021.9477382.

[34] K. Bespalova, E. Osterlund, G. Ross, M. Paulasto-Krockel, A.T. Sebastian, C.B. Karuthedath, S. Mertin, T. Pensala, Characterization of AlScN-Based Multilayer systems for piezoelectric micromachined ultrasound transducer (pMUT) fabrication, J. Microelectromechanical Syst. 30 (2021) 290–298, doi:10.1109/JMEMS.2021.3056928.

[35] R.C. Vickery, Scandium hydroxide and scandate ions, J. Chem. Soc. (1955) 251–255.

[36] P.A. Nikolaychuk, The revised potential-pH diagram of the Sc-H_2O system, Научные Ведомости Белгородского Государственного Университета. Серия: Естественные Науки. 25 (2016) 70–87.

[37] L.A. Pasechnik, A.G. Shirokova, O.V. Koryakova, N.A. Sabirzyanov, S.P. Yatsenko, Complexing properties of scandium(III) in alkaline medium, Russ. J. Appl. Chem. 77 (2004) 1070–1073, doi:10.1023/B:RJAC.0000044150.12253.3d.

[38] S. Fichtner, T. Reimer, S. Chemnitz, F. Lofink, B. Wagner, Stress controlled pulsed direct current co-sputtered $Al_{1-x}Sc_xN$ as piezoelectric phase for micromechanical sensor applications, APL Mater. 3 (2015) 116102, doi:10.1063/1.4934756.

[39] C.S. Sandu, F. Parsapour, S. Mertin, V. Pashchenko, R. Matloub, T. LaGrange, B. Heinz, P. Muralt, Abnormal grain growth in AlScN thin films induced by complexion formation at crystallite interfaces, Phys. Status Solid. 216 (2019) 1800569. 10.1002/pssa.201800569.

[40] C.S. Sandu, F. Parsapour, D. Xiao, R. Nigon, L.M. Riemer, T. LaGrange, P. Muralt, Impact of negative bias on the piezoelectric properties through the incidence of abnormal oriented grains in $Al_{0.62}Sc_{0.38}N$ thin films, Thin Solid Films 697 (2020) 137819, doi:10.1016/j.tsf.2020.137819.

[41] C. Liu, B. Chen, M. Li, Y. Zhu, N. Wang, Evaluation of the impact of abnormally orientated grains on the performance of ScAlN-based laterally coupled alternating thickness (LCAT) mode resonators and lamb wave mode resonators, 2020 IEEE Int. Ultrason. Symp., IEEE, 2020, doi:10.1109/IUS46767.2020.9251507.

[42] S. Mertin, V. Pashchenko, F. Parsapour, C. Nyffeler, C.S. Sandu, B. Heinz, O. Rattunde, G. Christmann, M.-A. Dubois, P. Muralt, Enhanced piezoelectric properties of c-axis textured aluminium scandium nitride thin films with high scandium content: Influence of intrinsic stress and sputtering parameters, in: 2017 IEEE Int. Ultrason. Symp, IEEE, 2017, pp. 1–4, doi:10.1109/ULTSYM.2017.8092187.

[43] S. Mertin, B. Heinz, O. Rattunde, G. Christmann, M.A. Dubois, S. Nicolay, P. Muralt, Piezoelectric and structural properties of c-axis textured aluminium scandium nitride thin films up to high scandium content, Surf. Coatings Technol. 343 (2018) 2–6, doi:10.1016/j.surfcoat.2018.01.046.

[44] D. Keogh, P. Asbeck, T. Chung, R.D. Dupuis, M. Feng, Digital etching of III-N materials using a two-step Ar/KOH technique, J. Electron. Mater. 35 (2006) 771–776, doi:10.1007/s11664-006-0137-6.

[45] D. Suh, Etch characteristics and morphology of Al_2O_3/TiO_2 stacks for silicon surface passivation, Sustain 11 (2019) 1–12, doi:10.3390/su11143857.

[46] M. Broas, O. Kanninen, V. Vuorinen, M. Tilli, M. Paulasto-Kröckel, Chemically stable atomic-layer-deposited Al_2O_3 films for processability, ACS Omega 2 (2017) 3390–3398, doi:10.1021/acsomega.7b00443.

[47] P.H. Chen, S. Wu, Y.C. Chen, J.L. Huang, D.F. Lii, Z.X. Lin, Microstructure and piezoelectric properties of c-axis ScAlN films on the Y-128° LiNbO3 substrate, Surf. Coatings Technol. 284 (2015) 129–132, doi:10.1016/j.surfcoat.2015.08.078.

[48] M. Clement, V.F. Jimena Olivares, T. Mirea, J. Olivares, E. Iborra, Effects of post-deposition vacuum annealing on the piezoelectric properties of AlScN thin films sputtered on 200 mm production wafers, 2018 IEEE Int. Ultrason. Symp, IEEE, 2018, doi:10.1109/ULTSYM.2018.8580177.

[49] M. Li, B. Chen, J. Xie, W. Song, Y. Zhu, Effects of post-annealing on texture evolution of sputtered ScAlN films, 2020 IEEE Int. Ultrason. Symp, IEEE, 2020, doi:10.1109/IUS46767.2020.9251741.